Supporting Information

Conjugated Microporous Polymer Network Grafted Carbon Nanotube Fibers with Tunable Redox Activity for Efficient Flexible Wearable Energy Storage

Wei Lyu,[†] Weiyi Zhang,[†] He Liu,[†] Yunpeng Liu,[‡] Hongyu Zuo,[†] Chunna Yan,[†] Charl F. J. Faul,[§] Arne Thomas,[‖] Meifang Zhu,[†] Yaozu Liao[†,*]

[†]State Key Laboratory for Modification of Chemical Fibers and Polymer Materials & College of Materials Science and Engineering, Donghua University, Shanghai 201620, China

[‡]Department of Environmental Engineering, Xi'an Jiaotong University, Xi'an, 710049, China

[§]School of Chemistry, University of Bristol, BS8 1TS, Bristol, UK

[‖] Department of Chemistry, Functional Materials, Technische Universität Berlin, Berlin 10623, Germany

Corresponding author
*E-mail: yzliao@dhu.edu.cn

Table of Contents

S1. Materials

Tris(4-bromophenyl)amine (TBA), phenylenediamine (PDA), 2,5-diaminopyridine dihydrochloride (2,5-DAP), 2,6-diaminoanthraquinone (2,6-DAQ), bis(dibenzylideneacetone) palladium(0) ($Pd(dba)_2$, 18-24% Pd), 2-dicyclohexylphosphino-2'4'6'-triisopropylbiphenyl (XPhos), 4-bromobenzenediazonium tetrafluoroborate, sodium tert-butoxide (NaOtBu,), dodecylbenzene sulfonic acid (DSA) and all the solvents with A.R. and C,R. grades were used as received and purchased from Tokyo Chemical Industry (TCI). Carbon nanotubes fibers (CNFs) were purchased from Chengdu Organic Chemicals Co. Ltd., Chinese Academy of Sciences and used as received (Physical property of the CNFs. Tensile strength: 310-500 Mpa; modulus: 4-6 GPa; elongation at break: 20-30%; density: 0.5-0.7 g cm^{-3}; electrical conductivity: $1*10^5$~$2*10^5$ S m^{-1}).

Section S2. Characterization and Measurements

S2.1 Materials Characterization

The morphologies of all fibers were characterized by a HITACHI S-4800 Scanning Electron Microscope and JEM-2100 Transmission Electron Microscopy. Fibers samples for TEM studies were prepared by dispersing scrap fibers into EtOH solution under ultrasonic irradiation for 12 h. Fourier transform infrared spectra (FT-IR) were performed on a Nicolet 670 spectrometer. Raman spectra were taken on an inVia-Reflex apparatus. An excitation wavelength of 633 nm for enhancing quinoid structure was used. N_2 adsorption/desorption measurements at 77.4 K were tested after degassing

samples under high vacuum at 120 °C for 15 h on a Micro ASAP 2016 instrument. Thermal gravimetric analysis (TGA) was measured on a TGA Q500 instrument under air and N_2 atmosphere in the temperature ranging from 30 to 800 °C, with heating rate of 10 °C min^{-1}. X-ray photoelectron spectra (XPS) were performed on an AVANCE400 spectrometer. ^{13}C CP/MAS spectra (NMR) of CMPs was recorded on an Agilent DD2 600 Solid NMR System with 4 mm zirconia rotors.

S2.2 Electrochemical characterization of individual fibers

Electrochemical measurements including electrochemical impedance spectroscopy (EIS), cyclic voltammetry (CV) and galvanostatic charge-discharge (GCD) were performed on a Gamry Interface1100E electrochemical workstation at room temperature in 0.5 M H_2SO_4 aqueous solution with a three-electrode cell, using individual fibers electrode, Pt wire and Ag/AgCl (3M KCl) as the working electrode, counter electrode and reference electrode, respectively. The EISs were investigated in the frequency ranging from 10^6 Hz to 0.01 Hz at open circuit voltage by applying a 5 mV signal. The specific areal capacitance (C_{sp}) of fibers in the three-electrode cell was calculated by the following equation (1):

$$C_{sp} = \frac{C_{electrode}}{A_{fiber}} \tag{1}$$

where $C_{electrode}$ is the measured capacitance in the three-electrode system and A_{fiber} stands for the surface area of the fiber which is considered as a cylinder. $C_{electrode}$ was calculated from the GCD by the presented equation (2):

$$C_{electrode} = \frac{I\Delta t}{\Delta V} \tag{2}$$

where I is the discharge current, Δt is the discharge time and ΔV is the potential window.

S2.3 Characterization of the flexible all-solid-state fibers-shaped symmetrical supercapacitors (FSCs)

The performance of the assembled FSCs was tested by CV and GCD in a two-electrode configuration on a Gamry Interface1100E electrochemical workstation at room temperature. For comparison, a symmetric-electrode test cell using two individual fibers in 0.5 M H_2SO_4 aqueous solution was also used. The capacitance of the FSCs (C_{cell}) in a two-electrode configuration was calculated from GCD curves at different current densities using the equation (3):

$$C_{cell} = \frac{I\Delta t}{\Delta V} \tag{3}$$

where I is the discharge current, Δt is the discharge time and ΔV is the potential window.

The areal, volumetric and gravimetric capacitances of the FSCs were calculated by the equations (4)-(6):

$$C_{cell,A} = \frac{C_{cell}}{A_{cell}} \tag{4}$$

$$C_{cell,V} = \frac{C_{cell}}{V_{cell}} \tag{5}$$

$$C_{cell,G} = \frac{C_{cell}}{M_{cell}} \tag{6}$$

where A_{cell} , V_{cell} and M_{cell} stand for the surface area, volume and mass of the effective region of FSCs device, respectively.

The specific areal capacitance of electrode materials in a two-electrode configuration was obtained by the equations (7):

$$C_{sp} = \frac{4C_{cell,A}}{A_{two}} \tag{7}$$

where A_{two} is the area of two active electrodes.

The specific gravimetric capacitance of active electrode materials (i.e. CMPs) in a two-electrode configuration was obtained by the equations (8):

$$C_{sp} = \frac{4C_{cell,G}}{M_{two}}$$

(8)

The areal energy density $E_{cell,A}$ and areal power density $P_{cell,A}$ were calculated from the equations (10)-(11):

$$E_{cell,A} = \frac{C_{cell,A}\Delta E^2}{2\times 3600} \tag{9}$$

$$P_{cell,A} = \frac{E_{cell,A}\times 3600}{t_{discharge}} \tag{10}$$

where ΔE is the operating voltage window in volts, $t_{discharge}$ is the discharge time.

S2.4 Electrode kinetics

The degree of capacitive effect for electrode was evaluated using Duun's and Trasati's method,[1] which is according to the following equations (11)-(12):

$$i = av^b \tag{11}$$

$$\log i = b\log v + \log a \tag{12}$$

where i is the current density, v is the scan rate, and a, b both are the variable parameters. b value was calculated by the slope of $\log v$ versus $\log i$ plot. Generally, b value of 0.5 represents a diffusion-controlled behavior and b value of 1 shows a capacitive-limited process.[2]

The capacitive contribution ratio under different scan rates was calculated by the equation (13) or (14):

$$i(V) = k_1 v + k_2 v^{1/2} \tag{13}$$

$$i(V)/v^{1/2} = k_1 v^{1/2} + k_2 v \tag{14}$$

where k_1 or k_2 is a constant for a given potential V. $k_1 v$ and $k_2 v^{1/2}$ represent the capacitance-limited and diffusion-limited contribution, respectively. $k_1 v$ and $k_2 v^{1/2}$ was calculated by plotting $i(V)/v^{1/2}$ versus $v^{1/2}$.

S2.5 Theoretical capacitance calculations

According to the proposed redox reaction mechanism of PTPA unit 1, four electrons can be obtained from the molecular weight of 378 g mol^{-1} repeating unit of PTPA.

The theoretical capacitance then can be calculated as following:[3]

$C_T = \frac{nF}{M_w * 3.6} = \frac{4*96485}{378*3.6} = 283.6 mAhg^{-1}$, where C_T is the theoretical capacitance, n is the electron transfer number, F is the Faraday constant, and M_w is the Molar weight.

Converting to Fg^{-1} : $C_T = \frac{283.6mAh}{g} * \frac{3600}{h} * \frac{A}{1000mA} = 1020Asg^{-1}$

Considering an operation window of 1.0 V studied in two-electrode cell: $C_T = \frac{1020As}{g} * \frac{1}{1.0} = 1020Fg^{-1}$

Section S3. Supplementary Figures and Tables

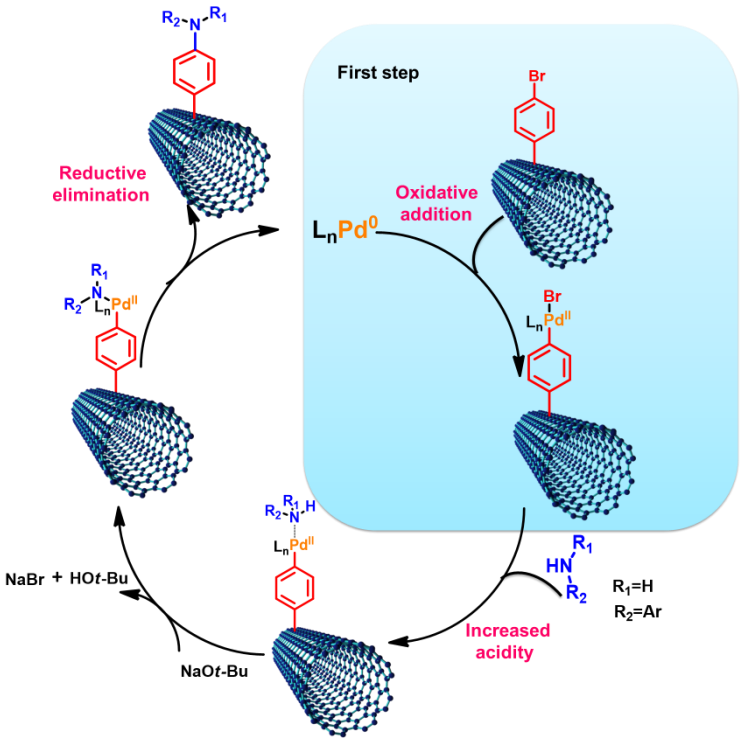

Figure S1 Mechanism of CNT-supported Buchwald Hartwig (BH) reaction. L: ligand. The first step where active palladium catalyst Pd^0 reacts with the aryl halide in an oxidation addition to produce a Pd^{II} intermediate is believed to be the rate-limiting step for Buchwald Hartwig coupling reaction. Here, CNF-Br fibers were placed in toluene solvent containing palladium catalyst Pd^0 for two hours to adsorb Pd^0, which can guarantee the effective transformation of Pd^0 to Pd^{II} in the next step and assure the BH coupling reactions on the CNT surface.

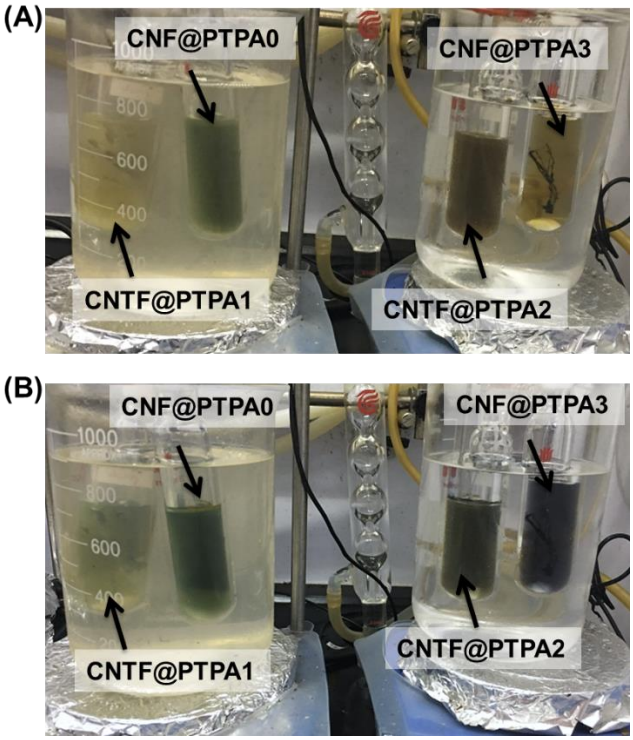

Figure S2 A-B) Photo images of BH reaction on raw CNF and CNF-Br fibers with different monomer and catalyst concentrations (i.e., CNF@PTPA0, CNF@PTPA1, CNF@PTPA2, CNF@PTPA3) at different reaction stages: after 1 h (A) and after 48 h (B). Although CNF@PTPA0 and CNF@PTPA1 synthesized using the same concentration of monomer and catalyst, the colors of reaction products were different. Meanwhile, with the decreased amount of monomer and catalyst, the BH reaction solution became gradually transparent, especially for CNF@PTPA3. Combined with the approximate grafting amount of PTPA on CNF-Br fibers for CNF@PTPA2 and CNF@PTPA3, we can deduce that the occurrence of BH reaction was mainly on the CNT-Br surface due to the pre-adsorbed Pd^0.

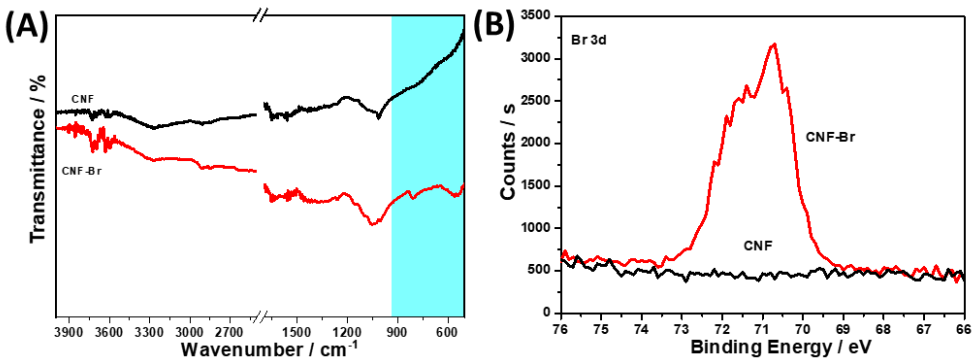

Figure S3 A）FT-IR spectra and B) high-resolution Br3d XPS spectra of CNF and CNF-Br. Compared with the FT-IR spectra of CNF, the new peaks located between 900-500 cm^{-1} corresponding to C-Br stretches can be observed for CNF-Br. Besides, after treated with *p*-bromobenzene diazonium salt, the characteristic peaks located around 71-72 eV accounting for the C-Br bonds appeared in Br3d XPS of CNF-Br, indicating the successful *p*-bromobenzene modification.

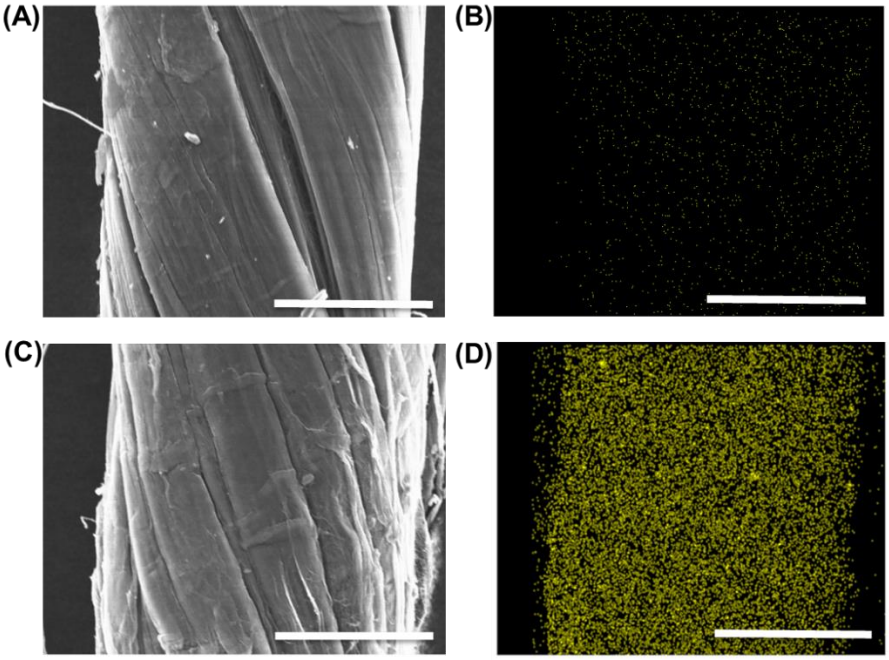

Figure S4 A, C) SEM images of CNF (A) and CNF-Br fiber (C) and B, D) the corresponding EDS mapping of Br element. Scale bars: 100 μm. Compared with negligible Br compositions observed in CNF, uniform and rich Br compositions distributed in CNF-Br fiber verified the successful *p*-bromobenzene modification.

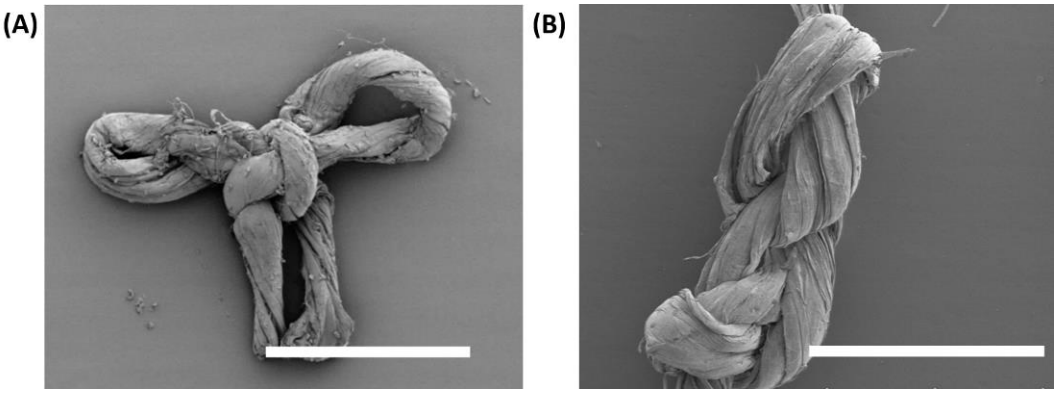

Figure S5 SEM images of CNF@CMPs fibers tied in different ways without obvious damage by using sharp tweezers. Scale bars: 1.00 mm.

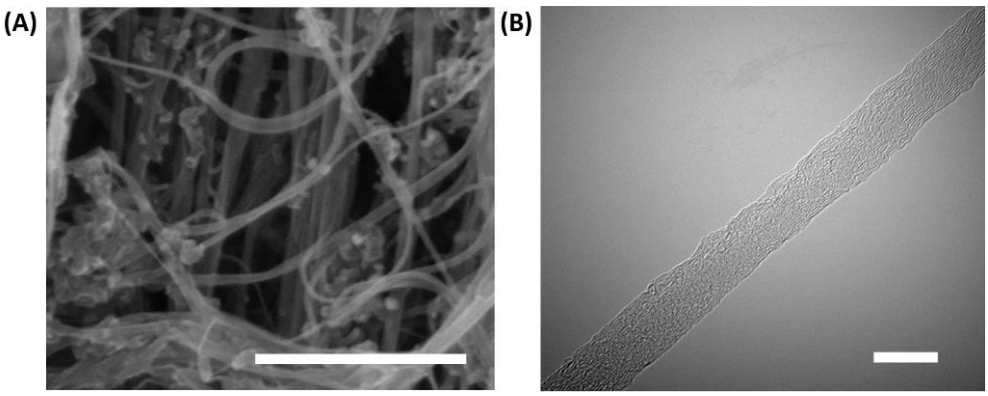

Figure S6 A) SEM and B) TEM images of CNT in raw CNF fibers. Scale bars: A) 500 nm and B) 10 nm.

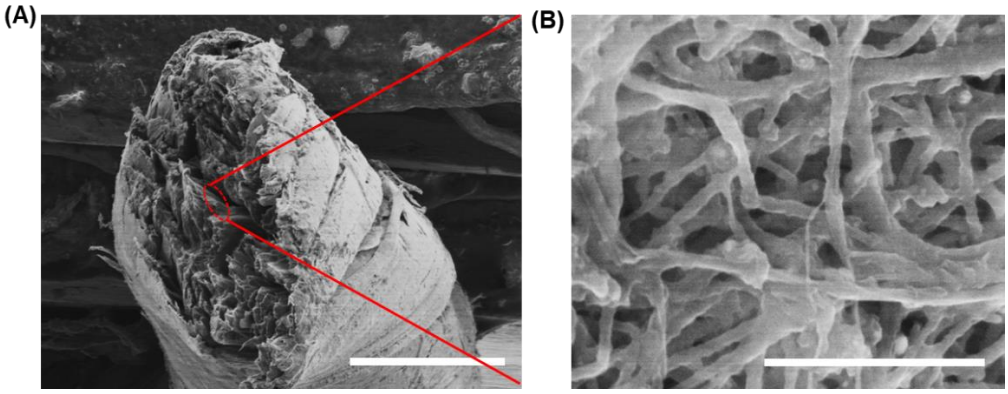

Figure S7 A) SEM images of the cross-section of CNF@PTPA3 and B) highlighted circle area (B). Scale bars: A) 100 μm and B) 500 nm.

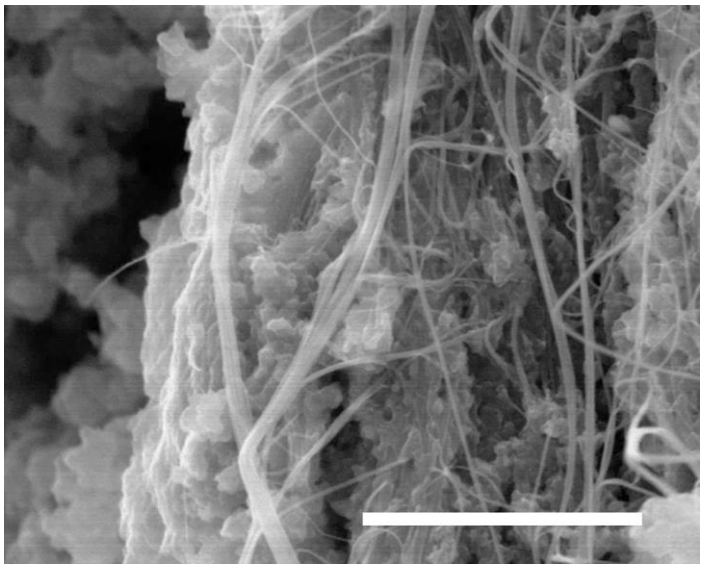

Figure S8 SEM image of CNF@PTPA0. Scar bars: 10 μm.

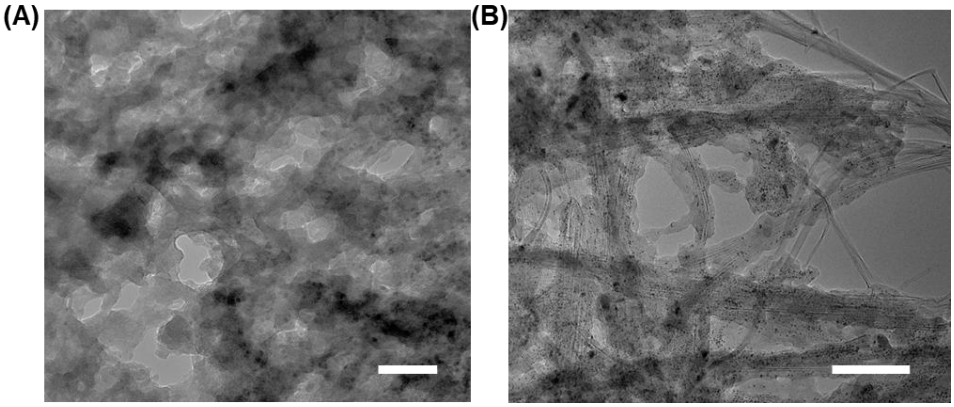

Figure S9 TEM images of different area of CNF@PTPA0. Scar bars: A) 50 nm and B) 200 nm.

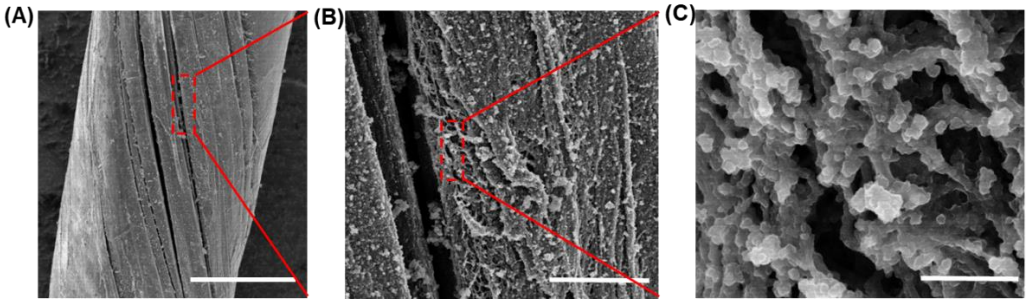

Figure S10 A-B) SEM images of the outer surface of CNF@PTPA2 at different magnifications and C) the selected inner area of CNF@PTPA2. Scar bars: A) 100 μm, B) 10.0 μm, and C) 1.00 μm.

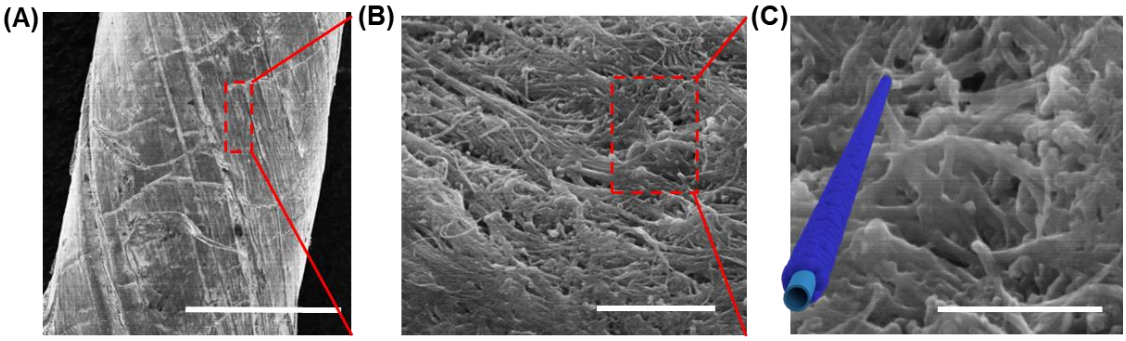

Figure S11 A-B) SEM images of the outer surface of CNF@PTPA3 at different magnifications and C) the selected inner area of CNF@PTPA3. Scar bars: A) 100 μm, B) 10.0 μm, and C) 1.00 μm.

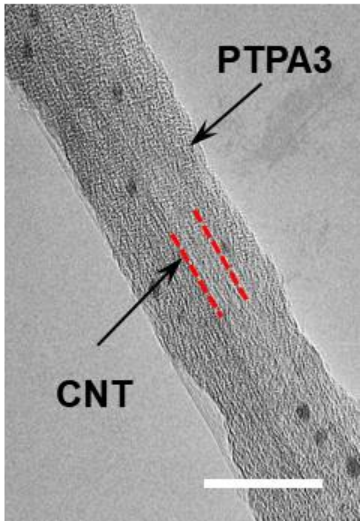

Figure S12 TEM images of CNF@PTPA3. Scar bars: 20 nm.

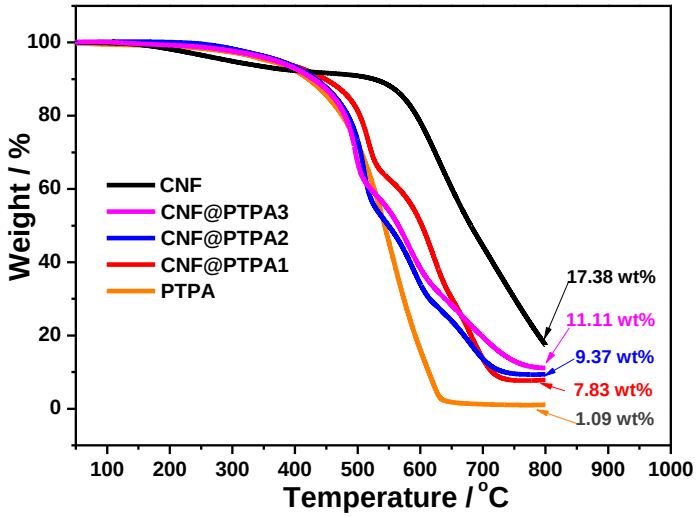

Figure S13 The TGA measurements of all the samples were carried out in air atmosphere. It is found that pure PTPA was decomposed nearly completely and a plateau was reached due to the residual Pd catalyst (~1.09 wt%) when the sample was heated to 800 ºC. The pure CNF exhibited a residue of 17.38 wt% at the same temperature. The CNF@PTPA1,2,3 showed residues of 7.83, 9.37, and 11.11 wt%, respectively. On the basis of these residues, the weight percentages of PTPA in CNF@PTPAs could be roughly calculated using the equation: $0.0109\ M_{CNF@PTPAs}\% + 0.1738\ (1-M_{CNF@PTPAs}\%) = M_{residual\ of\ CNF@PTPAs}\%$.

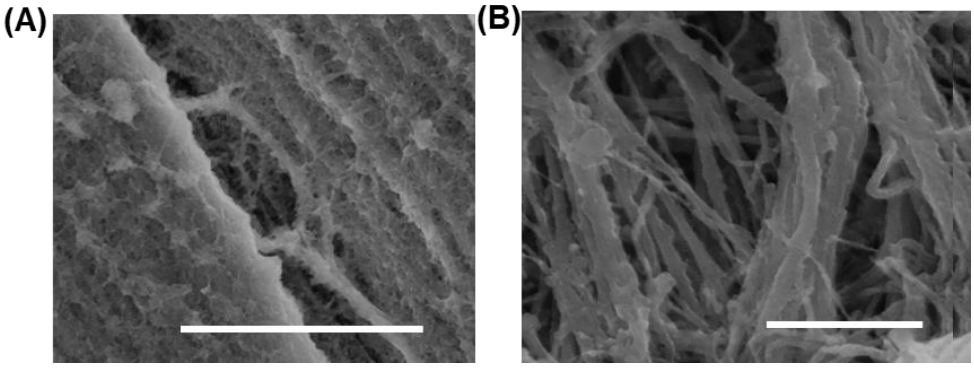

Figure S14 SEM images of A) CNF@PAPTA and B) CNF@PAQTA. Scale bars: A) 3.00 μm and B) 500 nm.

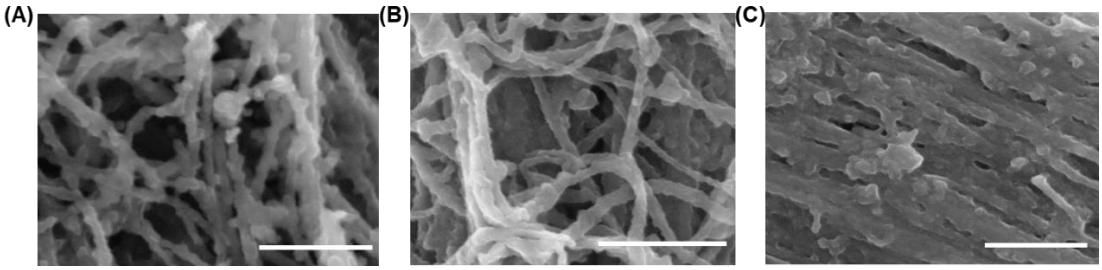

Figure S15 A-C) SEM images of CNF@PTPA2-X: A) CNF@PTPA2-100, B) CNF@PTPA2-200 and C) CNF@PTPA2-300, where X indicates the treated temperatures. Scale bars: 500 nm.

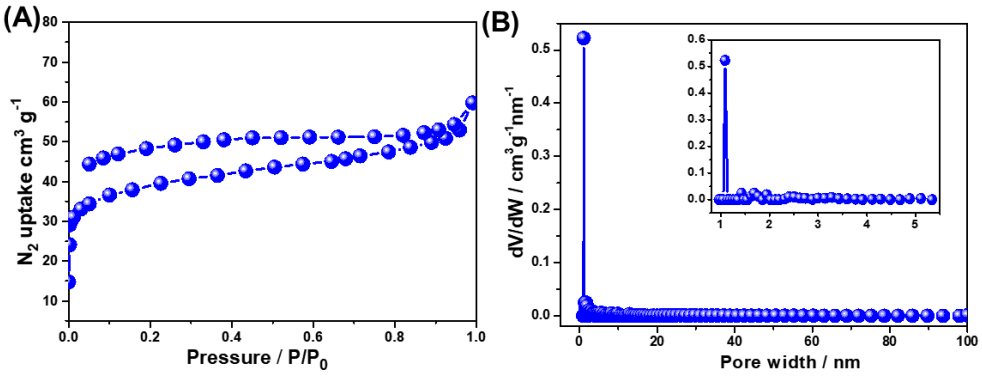

Figure S16 A) N_2 adsorption/desorption isotherms (77 K) and B) pore size distributions using DFT model of CNF@PTPA1.

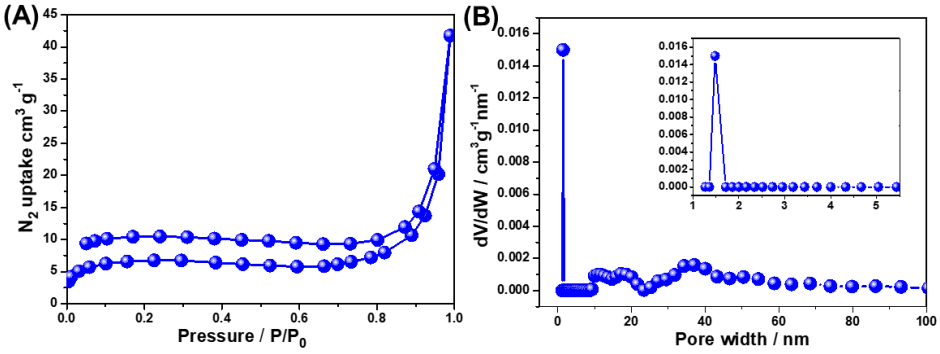

Figure S17 A) N_2 adsorption/desorption isotherms (77 K) and B) pore size distributions using DFT model of CNF@PTPA2.

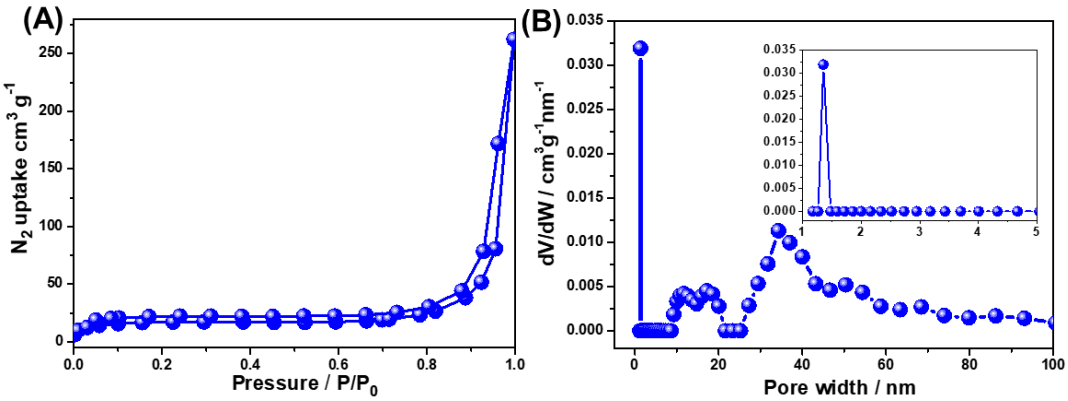

Figure S18 A) N_2 adsorption/desorption isotherms (77 K) and B) pore size distributions using DFT model of CNF@PTPA3.

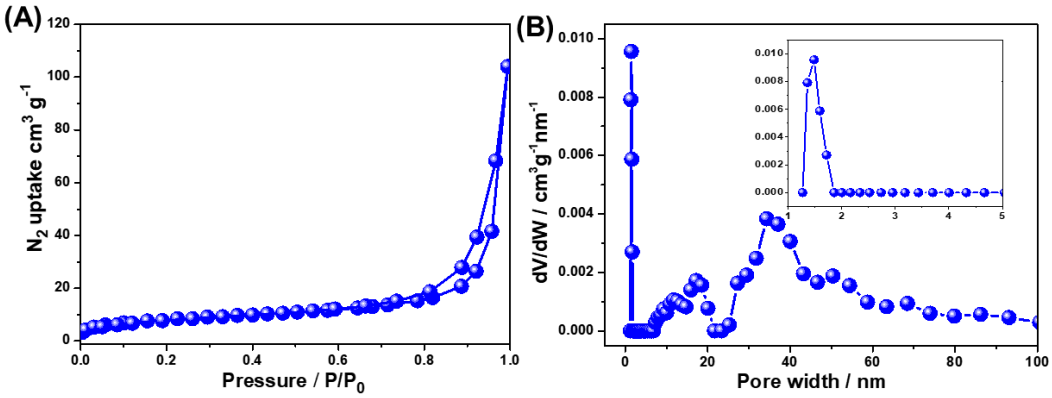

Figure S19 A) N_2 adsorption/desorption isotherms (77 K) and B) pore size distributions using DFT model of CNF@PAPTA.

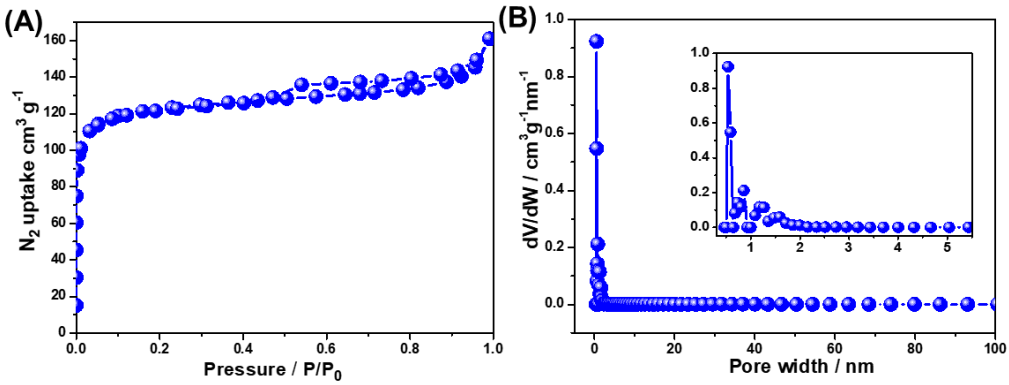

Figure S20 A) N_2 adsorption/desorption isotherms (77 K) and B) pore size distributions using DFT model of CNF@PAQTA.

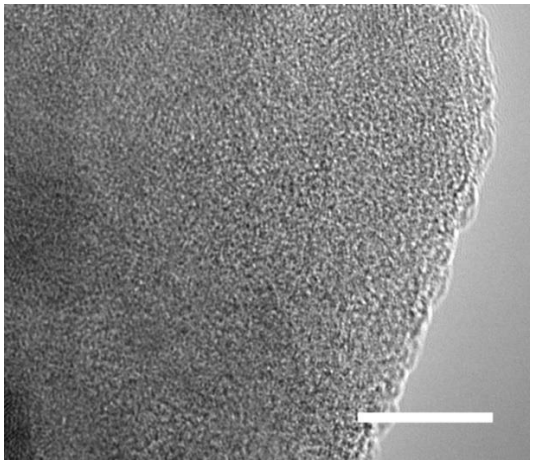

Figure S21 HRTEM images of PTPA. Scar bars: 10 nm.

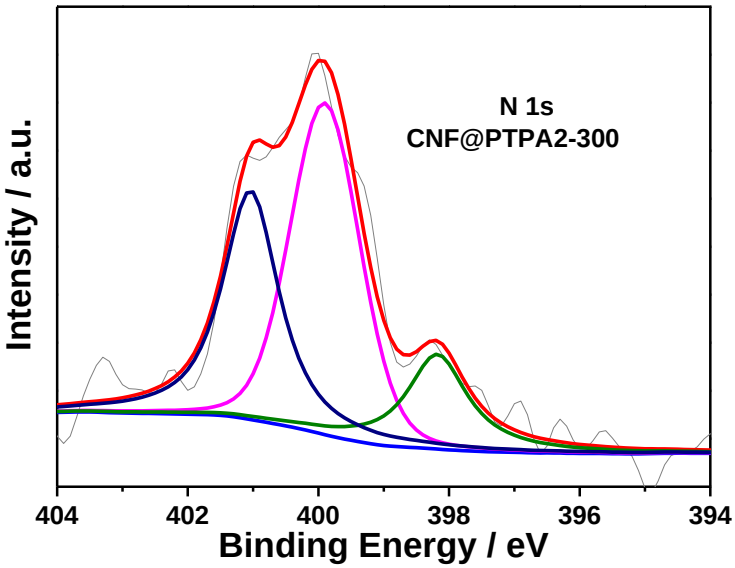

Figure S22 High-resolution N1s XPS spectra of CNF@PTPA2-300.

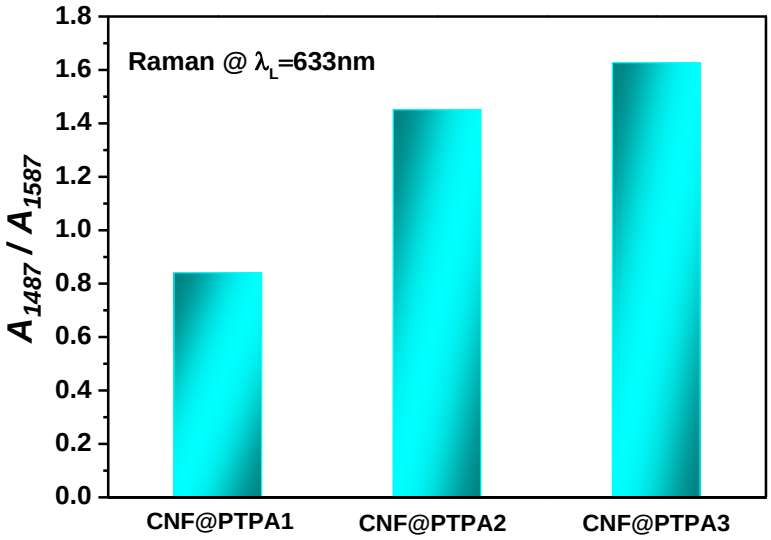

Figure S23 Ratio of A_{1487}/A_{1587} for CNF@PTPAs at excitation wavelength of 633 nm.

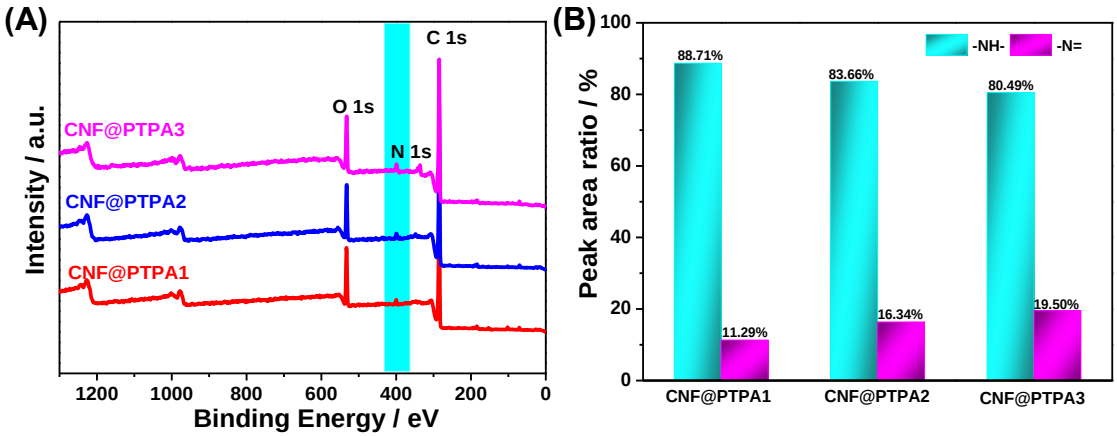

Figure S24 (A) Full-range XPS spectra and (B) peak area ratio of –NH- and –N= of CNF@PTPAs.

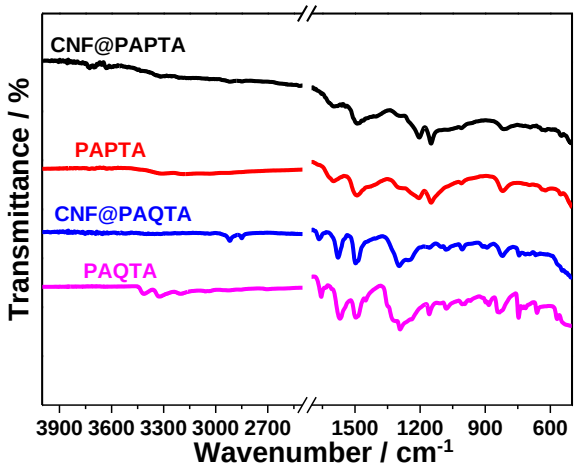

Figure S25 FTIR spectra of CNF@PAPTA, PAPTA, CNF@PAQTA and PAQTA.

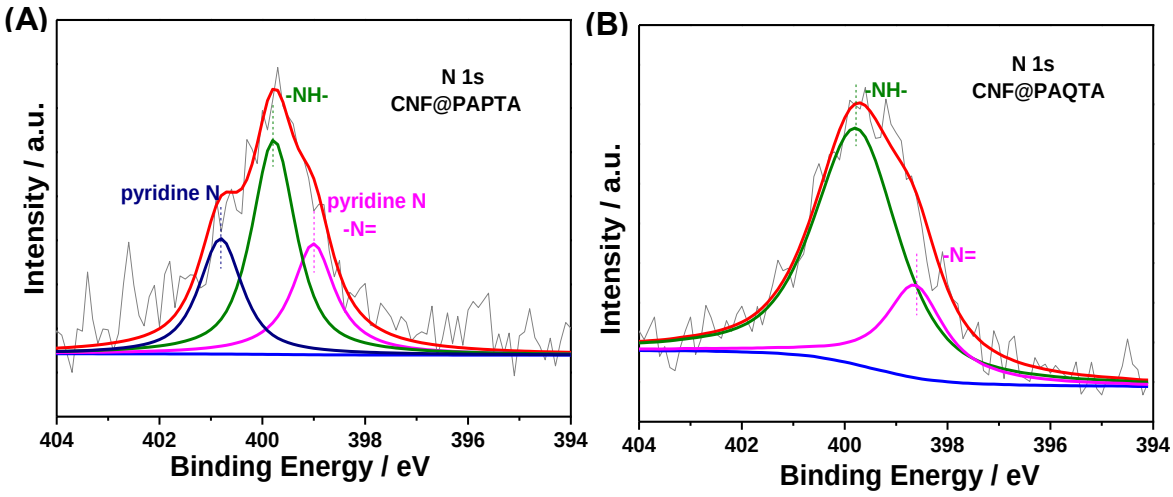

Figure S26 High-resolution N1s XPS spectra of CNF@PAPTA and CNF@PAQTA. 400.9 eV peak and 398.9 eV peak could be attributed to pyridine-N.[4]

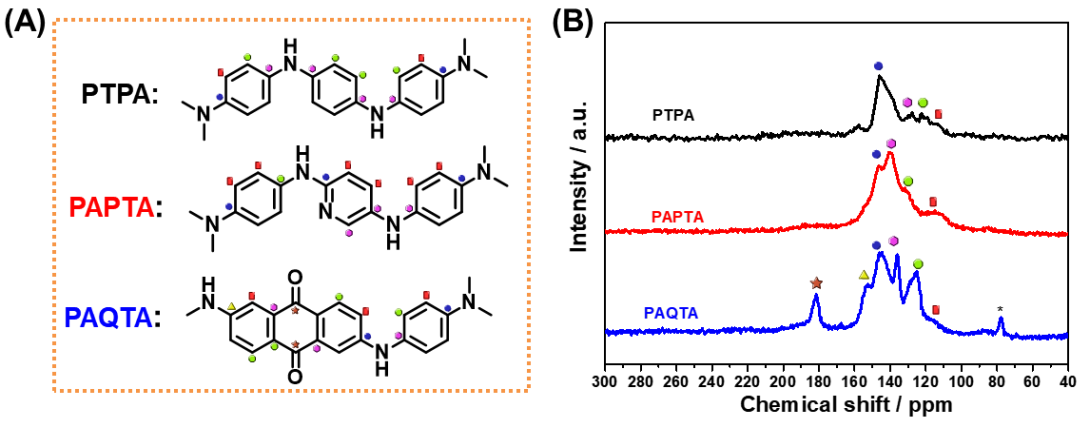

Figure S27 (A) Chemical structures and (B) solid-state ^{13}C CP/MAS NMR spectra of PTPA, PAPTA and PAQTA.

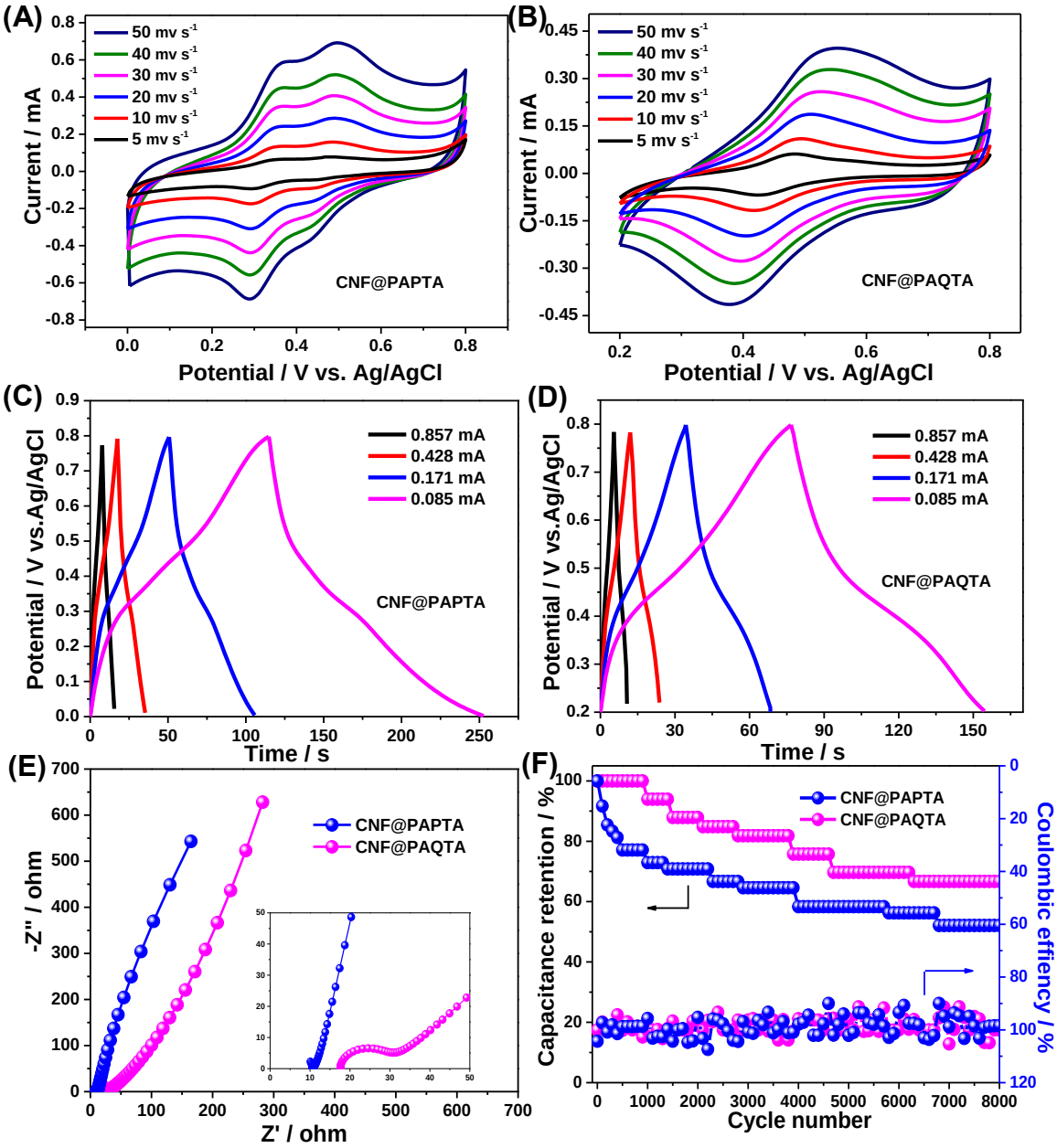

Figure S28 A-B) CV and C-D) GCD curves, Nyquist plot fitted with R(C(RW))(C(RW)) equivalent circuit and cycling life and Coulombic efficiencies of CNF@PAPTA and CNF@PAQTA fiber electrodes.

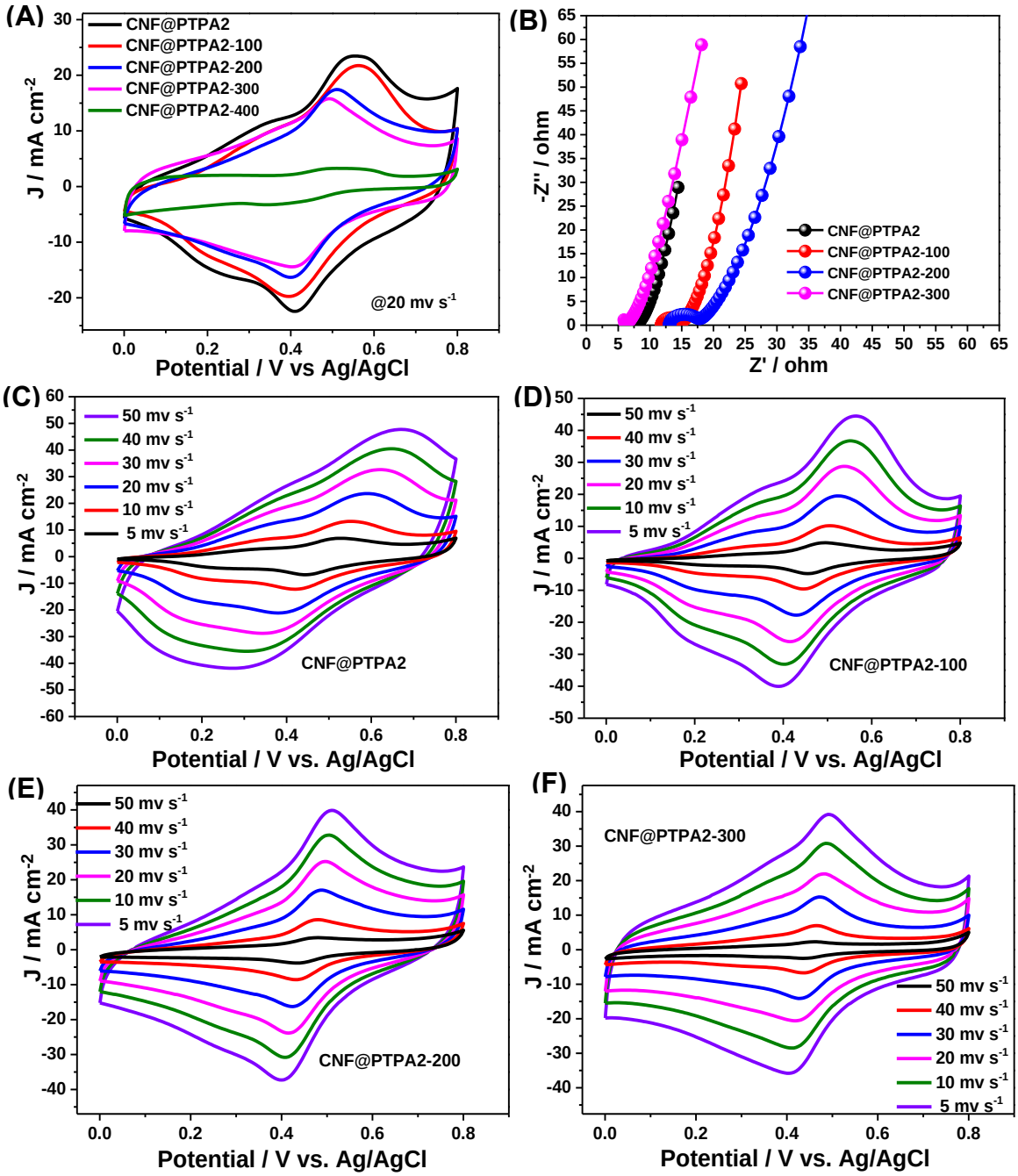

Figure S29 A) CV curves and B) Nyquist plot fitted with R(C(RW))(C(RW)) equivalent circuit of CNF@PTPA2 with different post-synthesis heat treatment; C-F) CV curves of C) CNF@PTPA2, D) CNF@PTPA2-100, E) CNF@PTPA2-200 and F) CNF@PTPA2-300 at various scan rates.

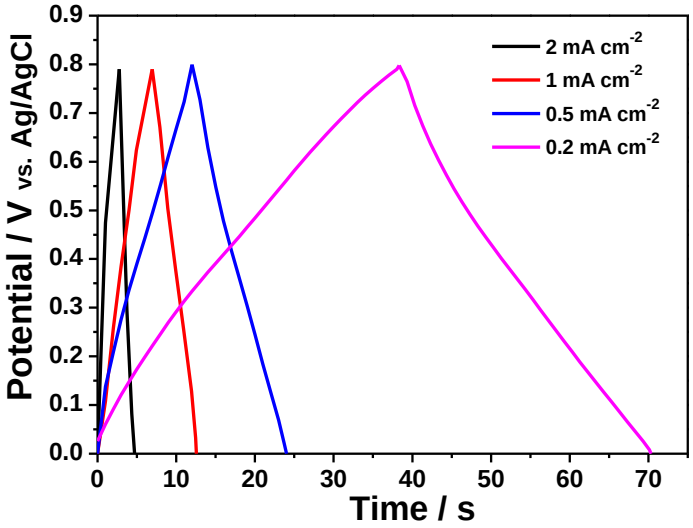

Figure S30 GCD curves of pure CNF electrode.

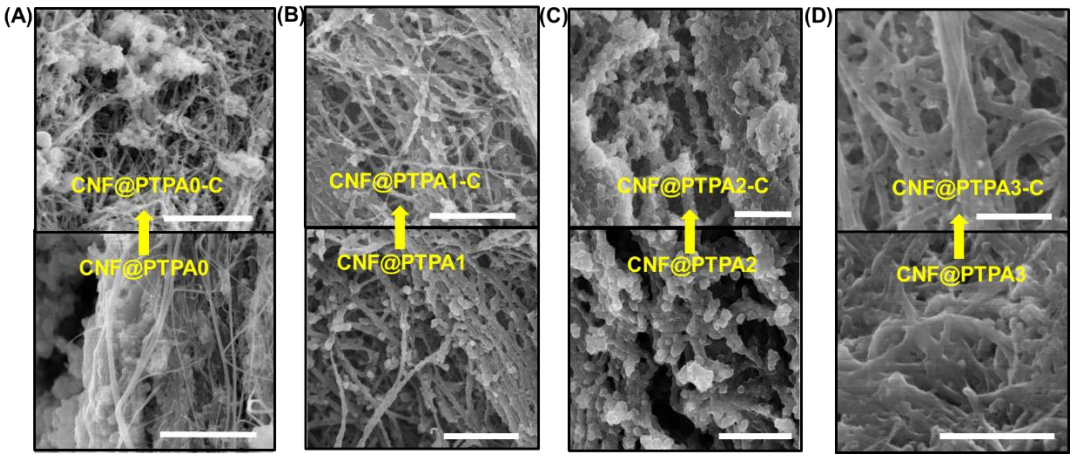

Figure S31 SEM images of CNF@PTPAs and CNF@PTPAs electrodes after 8000 GCD charging/discharging cycles (CNF@PTPAs-C): A) CNF@PTPA0, B) CNF@PTPA1, C) CNF@PTPA2, and D) CNF@PTPA3, scale bars: 1.00 μm.

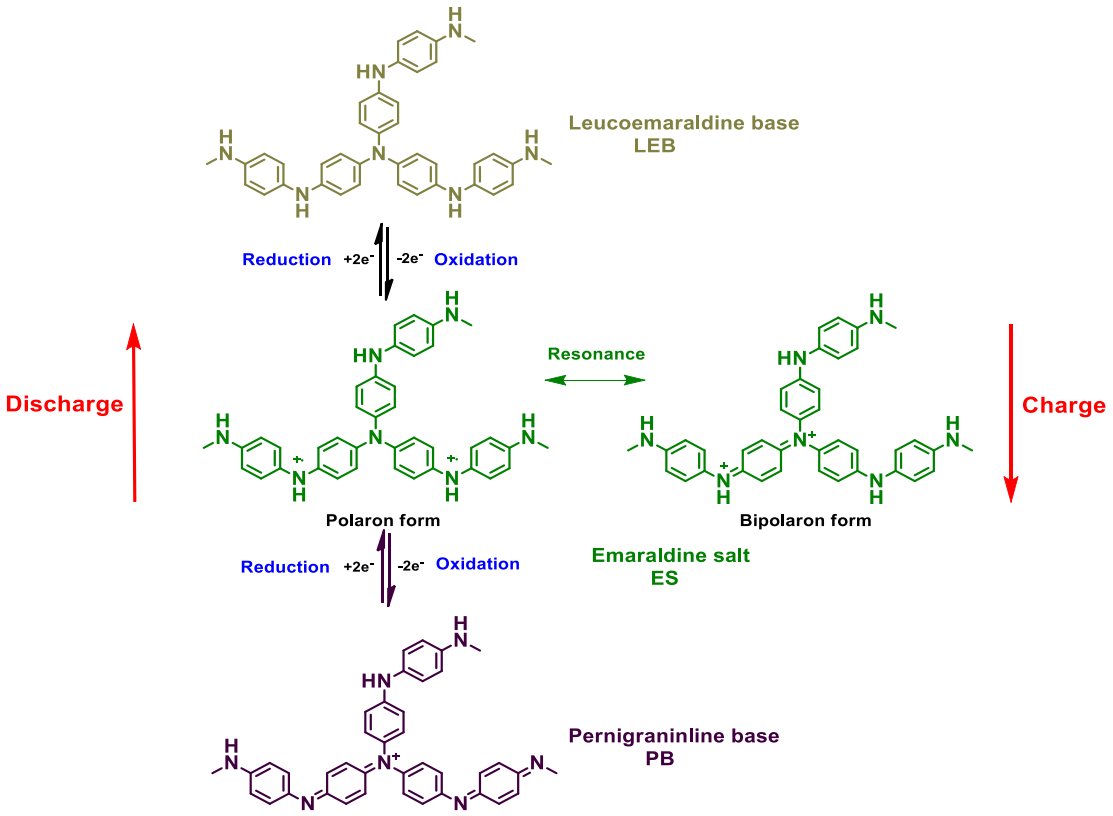

Figure S32 Proposed redox reactions, i.e., charge/discharge mechanism of PTPA. As PTPA forms polyaniline-like structure, the intrinsic leucoemeraldine base can be protonated and oxidized into a radical cation i.e.,polaron and then delocalized to a bipolaron with the loss of two electrons, leading to the formation of polyemeralidine. In the second step, further oxidation of polypemeralidine can form polypernigraline by losing another two electrons.[5]

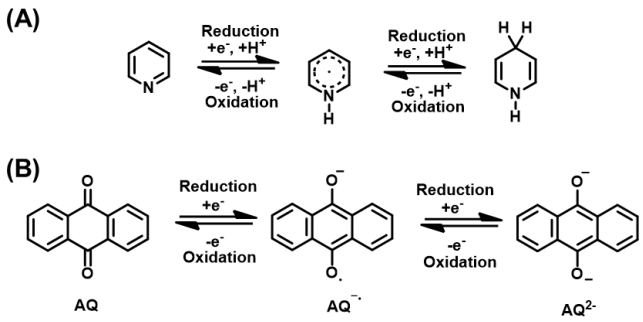

Figure S33 Proposed redox reactions, i.e., charge/discharge mechanism: A) pyridine[6] and B) anthraquinone.[7]

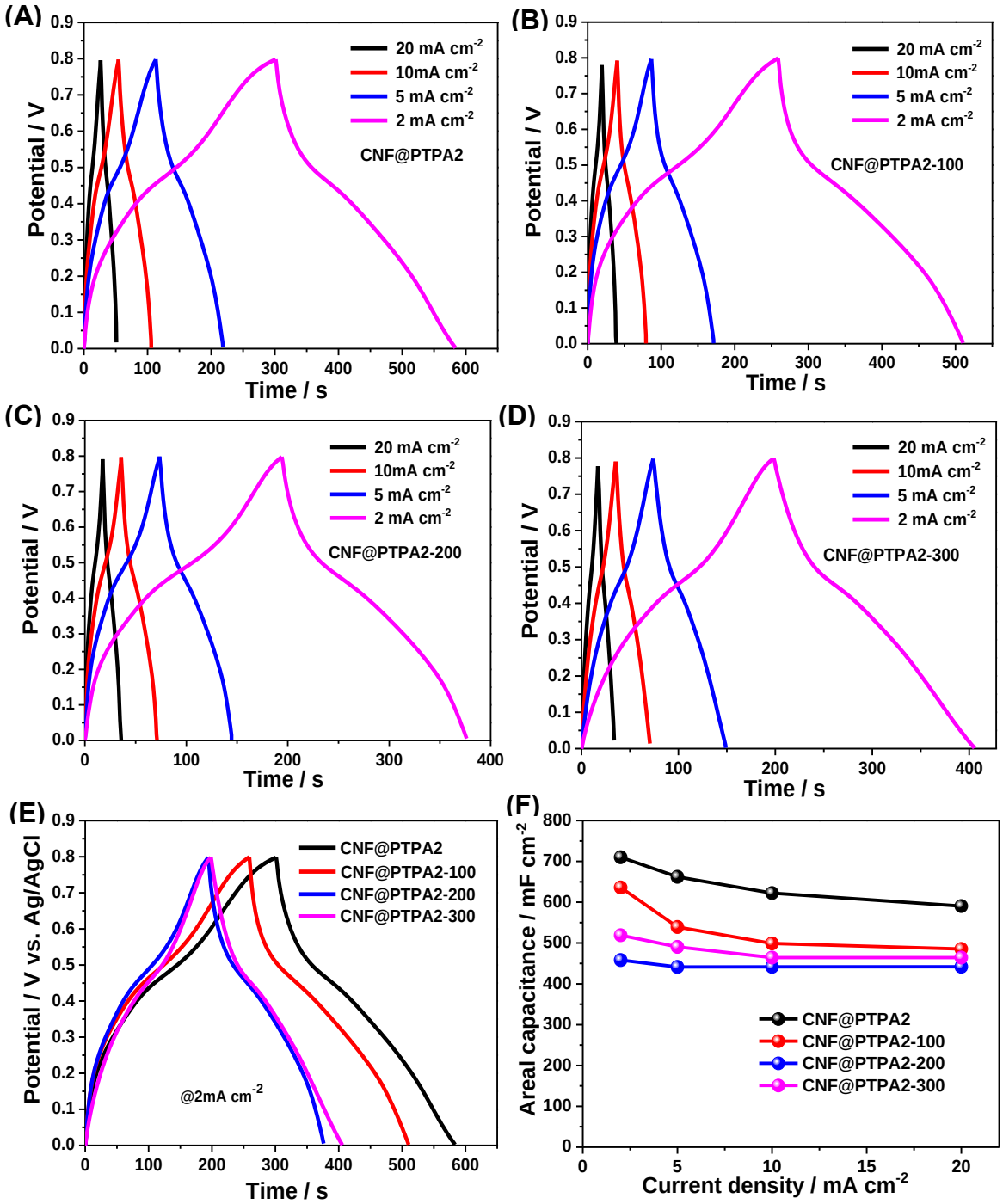

Figure S34 A-E) GCD curves and F) specific areal capacitance of CNF@PTPA2, CNF@PTPA2-100, CNF@PTPA2-200 and CNF@PTPA2-300 fiber electrodes.

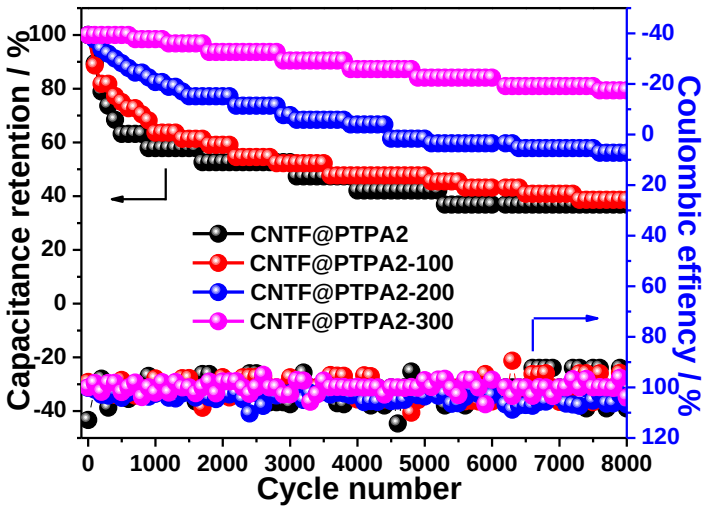

Figure S35 Cycling life and Coulombic efficiencies of CNF@PTPA2, CNF@PTPA2-100, CNF@PTPA2-200 and CNF@PTPA2-300 fiber electrodes.

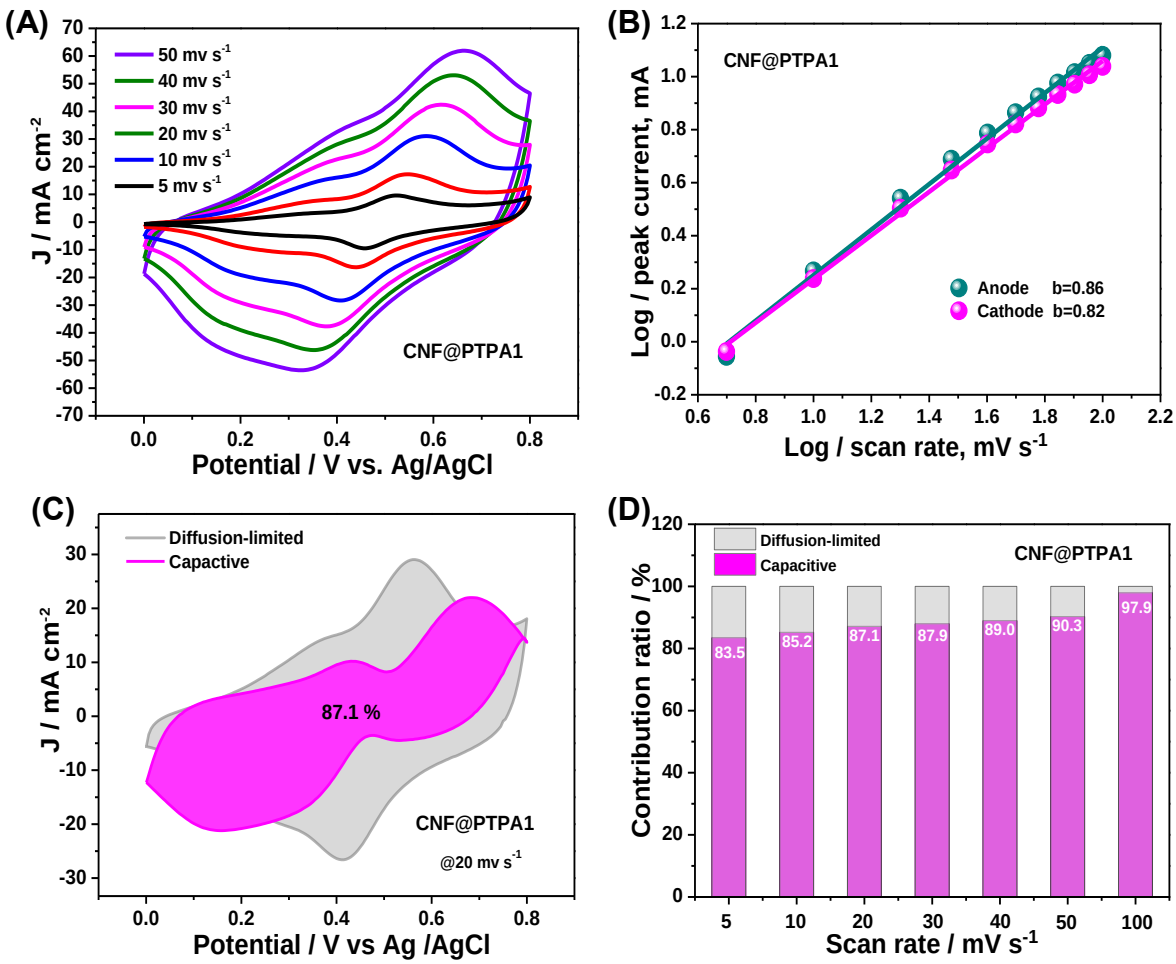

Figure S36 A) CV curves of CNF@PTPA1 fiber electrode at various scan rates, B) the relationship and fitted lines between Log(peak current) and Log(scan rates), C) separation of capacitive and diffusion currents, D) contribution ratios of capacitance-

and diffusion-limited processes of CNF@PTPA1 fiber electrode.

Table S1 Physical properties of CNF@PTPAs

Fiber	C_{PTA} **(mM)**	**Content of PTPA (wt%)**	**Fiber diameter (μm)**	**Density (mg/cm)**	**Charge transfer resistance (Ω)**[a]
CNF	0	0	160±10	0.116	4.6
CNF@PTPA1	1.25	58.64	200±10	0.200	8.5
CNF@PTPA2	0.938	49.14	190±10	0.173	7.2
CNF@PTPA3	0.625	38.51	180±10	0.159	6.6

[a]Calculated from Nyquist plot fitted with R(C(RW))(C(RW)) equivalent circuit in three-electrode cell.

Table S2. Comparison of loading amount of active materials in the CNF@PTPAs fiber electrodes with other conjugated polymer based fiber electrode.

Active material	Substrate	Mass loading amount	Ref.
PTPA	CNT fiber	38.51~49.14 wt%	**This work**
PANI	CNT fiber	70.00 wt%	8
PANI	GO fiber	73.10 wt%	9
GO/PPy	PLA fiber	0.121 mg cm^{-1} (72.40 wt%)	10
PANI	G/CNTs fiber	84.50 wt%	11

Table S3 The specific surface area and pore-structural parameters of CNF@CMPs

Sample	S_{BET}[a] / m^2 g^{-1}	V_{Total}[b] /cm^3 g^{-1}	V_{micro}[c] / cm^3g^{-1}
CNF@PTPA1	123.64	0.080	0.039
CNF@PTPA2	20.56	0.025	0.0078
CNF@PTPA3	52.88	0.096	0.018
CNF@PAPTA	28.64	0.050	0.0016
CNF@PTQTA	442.78	0.39	0.11

[a]Surface area calculated from nitrogen adsorption isotherms using the BET equation.
[b]Pore volume calculated from nitrogen adsorption at P/P_0 =0.95.
[c]Micropore volume calculated from t-plot method.

Table S4. Comparison of the electrochemical performance of CNF@PTPA3 FSCs with previously-reported conjugated polymer based FSCs.

Sample	Electrolyte	Specific capacitance ($mF\ cm^{-2}$)	Energy density ($\mu Wh\ cm^{-2}$)	Power Density ($mW\ cm^{-2}$)	Ref.
CNF@PTPA3	PVA/H_3PO_4	398.00 (88.4 $F\ cm^{-3}$)	18.33 (4.07 $mWh\ cm^{-3}$)	0.99 (220 $mWcm^{-3}$)	**This work**
PEDOT:PSS/PPy	PVA/H_2SO_4	770.6	16.20	0.7615	12
G/CNTs/PANI hollow fibers	$PVA\text{-}H_3PO_4$	472.00	14.00	0.12	11
PEDOT-S:PSS	$PVA/\ H_3PO_4$	93.1	8.30	0.4	13
PANI nanorods /GO	PVA/H_2SO_4	314.5	7.93	0.23	9
PEDOT/MnO_2/PEDOT sewing thread	PVA/LiCl	132.02	7.51	0.0523	14
Hollow rGO/PEDOT-PSS	$PVA/\ H_3PO_4$	304.5	6.8	0.0166	15
PEDOT:PSS@ rGO	PVA/H_3PO_4	131.00	4.55	0.125	16
PANI-HCNFs	PVA/H_3PO_4	123.20	4.28	0.00908	17
GO/PPy/PLA	$PVA\text{-}H_3PO_4$	158.80	3.50	0.032	10
RGO/CNTs@PANI	PVA/H_2SO_4	36.70 $F\ cm^{-3}$	0.98 $mWh\ cm^{-3}$	16.25 $mW\ cm^{-3}$	18

References

(1) Brezesinski, T.; Wang, J.; Tolbert, S. H.; Dunn, B. Ordered Mesoporous α-MoO_3 with iso-Oriented Nanocrystalline Walls for Thin-Film Pseudocapacitors. *Nat. Mater.* **2010**, *9*, 146-151.

(2) Wang, J.; Polleux, J.; Lim, J.; Dunn, B. Pseudocapacitive Contributions to Electrochemical Energy Storage in TiO_2(Anatase) Nanoparticles. *J. Phys. Chem. C* **2007**, *111*, 14925-14931.

(3) DeBlase, C. R.; Silberstein, K. E.; Truong, T.-T.; Abruña, H. D.; Dichtel, W. R. β-Ketoenamine-Linked Covalent Organic Frameworks Capable of Pseudocapacitive Energy Storage. *J. Am. Chem. Soc.* **2013**, *135*, 16821-16824.

(4) Eesley, G. L.; Burkstrand, J. M. X-ray-Photoemission and Raman Spectroscopy Investigation of Pyridine on Ag. *Phys. Rev. B* **1981**, *24(2)*, 582-585.

(5) a) Genies, E. M.; Lapkowski, M. Polyaniline Film. Electrochemical Redox Mechanisms. *Synthetic Met.* **1988**, *24*, 61-68; b) Genies, E. M.; Lapkowski, M.; Santier, C.; Vieil, E. Polyaniline, Spectroelectrochemistry, Display and Battery. *Synthetic Met.* **1987**, *18*, 631-636.

(6) Khattak, A. M.; Ghazi, Z. A.; Liang, B.; Khan, N. A.; Iqbal, A.; Li, L.; Tang, Z. A. Redox-Active 2D Covalent Organic Framework with Pyridine Moieties Capable of Faradaic Energy Storage. *J. Mater. Chem. A* **2016**, *4*, 16312-16317.

(7) Lin, K.; Chen, Q.; Gerhardt, M. R.; Tong, L.; Kim, S. B.; Eisenach, L.; Valle, A. W.; Hardee, D.; Gordon, R. G.; Aziz, M. J.; Marshak, M. P. Alkaline Quinone Flow Battery. *Science*, **2015**, *349*, 1529-1532.

(8) Chen, H.; Lin, H.; Deng, J.; Zhang, Y.; Sun, X.; Chen, P.; Fang, X.; Zhang, Z.; Guan, G.; Peng, H. Electrochromic Fiber-Shaped Supercapacitors. *Adv. Mater.* **2014**, *26*, 8126-8132.

(9) Zheng, X.; Yao, L.; Qiu, Y.; Wang, S.; Zhang, K.; Core-Sheath Porous Polyaniline Nanorodes/Graphene Fiber-Shaped Supercapacitors with High Specific Capacitance and Rate Capability. *ACS Appl. Energy Mater.* **2019**, *2*, 4335-4344.

(10) Nie, W.; Liu, L.; Li, Q.; Zhang, S.; Hu, J.; Yang, X.; Ding, X. A Wearable Fiber-Shaped Supercapacitor Based on a Poly(lactic acid) Filament and High Loading Polypyrrole. *RSC Adv.* **2019**, *9*, 19180-19188.

(11) Liu, K.; Chen, Z.; Lv, T.; Yao, Y.; Li, N.; Li, H.; Chen, T. A Self-supported Graphene/Carbon Nanotube Hollow Fiber for Integrated Energy Conversion and Storage. *Nano-Micro Lett.* **2020**, *12*, 64.

(12) Teng, W.; Zhou, Q.; Wang, X.; Che, H.; Hu, P.; Li, H.; Wang, J. Hierarchically Interconnected Conducting Polymer Hybrid Fiber with High Specific Capacitance for Flexible Fiber-Shaped Supercapacitor. *Chem. Eng. J.* **2020**, *390*, 124569.

(13) Wang, Z.; Cheng, J.; Guan, Q.; Huang, H.; Li, Y.; Zhou, J.; Ni, W.; Wang, B.; He, S.; Peng, H. All-in-One Fiber for Stretchable Fiber-Shaped Tandem Supercapacitors. *Nano Energy* **2018**, *45*, 210-219.

(14) Gao, X.; Xiao, X.; Dong, B.; Hu, J.; Tang, S.; Qi, W.; Zou, D. Converting Commercial Sewing Threads into High-Performance and Flexible/Wearable Fiber-Shaped Supercapacitors via Facile Vapor Deposition Polymerization. *ChemistrySelect* **2019**, *4*, 5355-5365.

(15) Qu, G.; Cheng, J.; Li, X.; Yuan, D.; Chen, P.; Chen, X., Wang, B.; Peng, H. A Fiber Supercapacitor with High Energy Density Based on Hollow Graphene/Conducting Polymer Fiber Electrode. *Adv. Mater.* **2016**, *28*, 3636-3652.

(16) Li, B.; Cheng, J.; Wang, Z.; Li, Y.; Ni, W.; Wang, B. Highly-Wrinkled Reduced Graphene Oxide-Conductive Polymer Fibers for Flexible Fiber-Shaped and Interdigital-Designed Supercapacitors. *J. Power Sources* **2018**, *376*, 117-124.

(17) Yang, D.; Ni, W.; Cheng, J.; Wang, Z.; Li, C.; Zhang, Y.; Wang, B. Omnidirectional Porous Fiber Scrolls of Polyaniline Nanopillars Array-N-doped Carbon Nanofibers for Fiber-Shaped Supercapacitors. *Mater. Today Energy* **2017**, *5*, 196-204.

(18) Liu, D.; Du, P.; Wei, W.; Wang, H.; Wang, Q.; Liu, P. Skeleton/Skin Structured (RGO/CNTs)@PANI Composite Fiber Electrodes with Excellent Mechanical and Electrochemical Performance for All-Solid-State Symmetric Supercapacitors. *J Colloid Interface Sci.* **2018**, *513*, 195-303.